

We are IntechOpen, the world's leading publisher of Open Access books Built by scientists, for scientists

7,000

Open access books available

186,000

International authors and editors

200M

Downloads

Our authors are among the

154

Countries delivered to

TOP 1%

most cited scientists

12.2%

Contributors from top 500 universities



WEB OF SCIENCE™

Selection of our books indexed in the Book Citation Index
in Web of Science™ Core Collection (BKCI)

Interested in publishing with us?
Contact book.department@intechopen.com

Numbers displayed above are based on latest data collected.
For more information visit www.intechopen.com



Algebraic Reconstruction and Post-processing in Incomplete Data Computed Tomography: From X-rays to Laser Beams

Alexander B. Konovalov, Dmitry V. Mogilenskikh, Vitaly V. Vlasov and
Andrey N. Kiselev
*Russian Federal Nuclear Centre – Zababakhin Institute of Applied Physics
Russia*

1. Introduction

Methods of computed tomography are well developed and widely used in medicine and industry. If tomographic data are complete, it is possible to reconstruct the images with sub-millimeter resolution. If the data are incomplete, tomograms may blur, i.e. their resolution degrades, noise increases and artifacts form. The situation is worst if measurement data are so poor that the system of equations which describe the discrete reconstruction problem appears to be strongly underdetermined. In this situation, images of acceptable quality can be obtained with algorithms that regularize the solution and use a priori information about the object, and do post-processing of reconstructed tomograms also with the use of a priori information, as a rule. This chapter provides two examples demonstrating the reconstruction of the internal structure of an object from strongly incomplete measurement data: few-view computed tomography (FVCT) and diffuse optical tomography (DOT) of strongly scattering media. The problem of reconstruction from a small number of views (<10) arises, for example, in experimental plasma research (Pickalov & Melnikova, 1995) or nondestructive testing (Subbarao et al., 1997). DOT is now deemed to hold much promise for cancer detection (Arridge, 1999; Hawrysz & Sevick-Muraca, 2000; Yodh & Chance, 1995). Here the strong incompleteness of data is caused by the fact that the number of source-receiver relations that define the number of measurements is strictly limited. Despite that these types of tomography use different wavelength bands (X-ray and near infrared) and different mathematical models (linear and non-linear), we think it is not only possible, but also interesting to consider them together because in both cases we successfully use similar reconstruction algorithms and similar post-processing methods. The unique possibility to do that comes from the fact that in case of DOT, we use a simplified reconstruction method (Konovalov et al., 2003; 2006b; 2007; Lyubimov et al., 2002; 2003) reducing the inverse problem to a solution of the integral equation with integration along a conditional photon average trajectory (PAT) – an analog of the Radon transform in projection tomography.

In case of FVCT, we use actual data from measurements in a simple experimental radiography setup (Konovalov et al., 2006a). The FVCT procedure is simulated by rotation of the object from exposure to exposure about the centre of the reconstruction region. For

objects, we use a spatial resolution test and an iron sphere with quasi-symmetric cracks resulted from shock compression.

In case of DOT, we use model data from the numerical solution of a time-dependent diffusion equation with an instantaneous point source (time-domain measurement technique). We consider a traditional geometry where sources and receivers are on the boundary of a scattering object in the form of a flat layer (Konovalov et al., 2006b). The object contains periodic structures created by circular absorbing inhomogeneities.

In both cases, the inverse problem is solved using algebraic reconstruction techniques (additive and multiplicative) which we modernized to attain the better convergence of the iterative reconstruction process (Konovalov et al., 2006a; 2006b). Procedures used to calculate the weight matrices are described in detail. Solution correction formulas are modified with respect to distributions of weight sums and solution correction numbers over image elements. Weighted smoothing is performed at each iteration of solution approximation. We use a priori information on whether the solution is non-negative and on the presence of structure-free zones in the reconstruction region.

For post-processing of reconstructed tomograms, we use space-varying restoration (Konovalov et al., 2007), methods for enhancing informativity of images based on its nonlinear color interpretation (Mogilenskikh, 2000) and methods for estimating image informativity based on binary operations and visualization algorithms (Mogilenskikh & Pavlov, 2002; Mogilenskikh, 2003).

Results of investigation help decide how spatial resolution depends on the degree of data incompleteness and draw inferences on whether the modified reconstruction techniques are effective and on the investigated post-processing methods are capable of making tomograms more informative.

The chapter is organized as follows. Section 2 gives a general formulation of the tomography problem. It is shown that the inverse problem of DOT, like the problem of reconstruction from X-ray projections, can be reduced to a solution of an integral equation with integration along the trajectory. The Section describes a discrete model of a 2D reconstruction problem and modernized algebraic techniques. Section 3 gives examples of 2D reconstruction from experimental radiographic data and model diffusion projections from optical inhomogeneities. The Section makes a quantitative analysis of the spatial resolution of tomograms reconstructed from strongly incomplete data. Section 4 describes post-processing methods and gives examples of their use. Section 5 draws inferences and outlines further research in the area.

2. Generality of our approach to reconstruction from strongly incomplete data

2.1 From the Radon transform to the fundamental equation of the PAT method

The problem of reconstruction in computed tomography is known to be formulated as follows: find the best estimation of a function of spatial coordinates $f(\mathbf{r})$, called an object function, from a discrete set of its measured projections. Generally, each projection can be written as a weighting integral

$$g = \int_{\infty} w(\mathbf{r}) f(\mathbf{r}) d^3r, \quad (1)$$

where $w(\mathbf{r})$ is a weighting function which depends on source and receiver positions in space, the type of actual physical measurements and the way of data recording.

In transmission X-ray tomography where the spatial distribution of the extinction coefficient $\mu(\mathbf{r})$ is reconstructed, it is usually assumed that the weighting function is unity along a line L connecting a point source and a point receiver, and zero elsewhere. Then expression (1) turns into the linear integral

$$g = \int_L \mu(\mathbf{r}) dl. \quad (2)$$

In computed tomography, it is known as the Radon transform. Integral (2) is inverted with a linear reconstruction model implemented with the use of both integral algorithms (Kak & Slaney, 1988) and algebraic techniques (Herman, 1980).

Divergence of the probing beam in, for example, proton (Hanson, 1981; 1982) or diffraction (Devaney, 1983) tomography makes it necessary to consider not a line but a narrow 3D strip of a finite length. In this case, it may be needed to change from linear integration (2) to volume one (1) and pose restrictions on the use of the linear reconstruction model.

Diffuse optical tomography (DOT) of strongly scattering media is the most demonstrative example of non-linear tomography. Laser beams used for probing undergo multiple scattering, so photon trajectories are not regular and photons are distributed in the entire volume V under study. As a result, each point in the volume significantly contributes to the detected signal. If, for example, we deal with absorbing inhomogeneities of tissues examined by pulsed probing with the time-domain measurement technique, integral (1), in the approximation of the perturbation theory by Born or Rytov, takes the form (Lyubimov et al., 2002; 2003)

$$g(t) = \int_V \left\{ \int_0^t v P[\mathbf{r}, \tau | (\mathbf{r}_s, 0) \rightarrow (\mathbf{r}_d, t)] d\tau \right\} \delta\mu_a(\mathbf{r}) d^3r, \quad (3)$$

where t is the time-gating delay of the receiver recording the signal, v is the light velocity in the media, $P[\mathbf{r}, \tau | (\mathbf{r}_s, 0) \rightarrow (\mathbf{r}_d, t)]$ is the density of the conditional probability that a photon migrating from a space-time source point $(\mathbf{r}_s, 0)$ to a space-time receiver point (\mathbf{r}_d, t) reaches an intermediate space point \mathbf{r} at time τ , and $\delta\mu_a(\mathbf{r})$ is the distribution function of the absorbing inhomogeneities. Local linearization of the inverse problem of DOT is usually done with multi-step reconstruction algorithms based on the variational formulation of the radiation transport equation (or its diffusion approximation). The Newton-Raphson algorithm with the Levenberg-Marquardt iterative procedure (Arridge, 1999) is a typical example of these algorithms. The multi-step algorithms provide a relatively high spatial resolution (~ 5 mm) for diffusion tomograms, but they are not as fast as required for real-time diagnostics because we have to solve a forward problem, i.e. the problem of propagation of radiation through matter, many times by adjusting at each linearization step the matrix of coefficients of a system of algebraic equations describing the discrete reconstruction model.

There is a unique opportunity to accelerate the reconstruction procedure: to change in expression (3) from volume integration to integration along a conventional line connecting point source and point receiver. Using a probabilistic interpretation of light transfer by

means of the conditional probability density P , Lyubimov et al. (2002; 2003) proved that integral (3) could be presented as

$$g(t) = \int_L \frac{\langle \delta\mu_a(\mathbf{r}) \rangle_P}{v(l)} dl, \quad (4)$$

where L is a curve defined by coordinates of the mass centers of the instantaneous distributions P in accordance with

$$\mathbf{R}(\tau) = \int_V \mathbf{r} P[\mathbf{r}, \tau | (\mathbf{r}_s, 0) \rightarrow (\mathbf{r}_d, t)] d^3r, \quad (5)$$

which we call a photon average trajectory (PAT). Here l is a distance along the PAT, $v(l)$ is the relative velocity of the mass center of the distribution P along the PAT as a function of l , $\langle \cdot \rangle_P$ is the operator of averaging over the spatial distribution P . Integral equation (4) is a fundamental equation of the photon average trajectories method (PAT method) in case of time-domain measurement technique. It is an analog of Radon transform (2) and can be inverted with the fast algorithms of projection tomography. In other words, converting (3) into (4) offers an opportunity to change from multi-step to one-step reconstruction in the sense that the system of algebraic equations describing the discrete reconstruction model is only inverted once and hence, to achieve significant savings in computational time.

Equation (4) has definitely a number of differences from equation (2), specifically:

- (a) Integration is performed along not a straight but curved line;
- (b) Under integral (4), there is a weighting distribution $1/v(l)$ which depends on spatial coordinates; and
- (c) Trajectory integration is applied not to the object function itself, but to a function averaged over the spatial distribution P .

The latter means that the reconstructed image is degraded by a priori blur which requires additional work, i.e. post-processing of tomogram. With the above differences, it becomes clear that the inversion of equation (4) with the linear reconstruction model requires certain assumptions which may affect the quality of reconstructed images. Nevertheless, our earlier studies (Konovalov et al., 2003; 2006b; 2007; Lyubimov et al., 2002; 2003) and results presented in Sections 3 and 4 show that the PAT method is quite effective in the context of the tomogram quality versus reconstruction speed trade-off.

2.2 Discrete image reconstruction model

In medical applications of X-ray computed tomography, equation (2) is usually inverted by means of integral reconstruction algorithms such as the backprojection algorithm with convolution filtering (Kak & Slaney, 1988). In FVCT where the number of views is small, reconstruction with the integral algorithms gives aliasing artifacts which are present on tomograms as "rays" tangential to reproduced structures (Palamodov, 1990). Different smoothing and regularization methods can be applied to remove these artifacts which strongly restrict the resolution of small details. But the quality of reconstructed images still remains far from satisfactory.

It is also difficult to invert equation (4) with integral algorithms. Here problems arise from not only incomplete data, but also from curved PATs. Our attempts to implement the

backprojection algorithm for diffusion tomograms (Konovalov et al., 2003; 2007; Lyubimov et al., 2003) are based on the assumption that the PATs are almost straight lines inside the scattering object. But with this approach it is impossible to reconstruct the spatial distribution of absorbing inhomogeneities near boundaries where photons escape from the object like an avalanche and the PATs strongly bend.

In this case, both in FVCT and in DOT, it is appropriate to use iterative algebraic algorithms implementing a discrete reconstruction model. In this chapter, without loss of generality, we will only consider examples of 2D reconstruction, i.e. reconstructions of 2D images. The generalized discrete model of 2D reconstruction is formulated traditionally (Herman, 1980). Let us establish a Cartesian grid for square image elements so that it covers the object. Assume that the reconstructed object function takes a constant value f_{kl} in an element with indices k and l (hereafter, (k, l) -cell). Let L_{ij} be a straight line or PAT connecting i -source and j -receiver, and g_{ij} be a projection measured by j -receiver from i -source. Then the discrete reconstruction model can be characterized by a system of linear algebraic equations

$$g_{ij} = \sum_{k,l} W_{ijkl} f_{kl}, \quad (6)$$

where W_{ijkl} is the weight contributed by the (k, l) -cell to the measured value g_{ij} . In the traditional setup of 2D reconstruction, the weight W_{ijkl} is proportional to the length of intersection of the trajectory L_{ij} with the (k, l) -cell (Herman, 1980; Lyubimov et al., 2002).

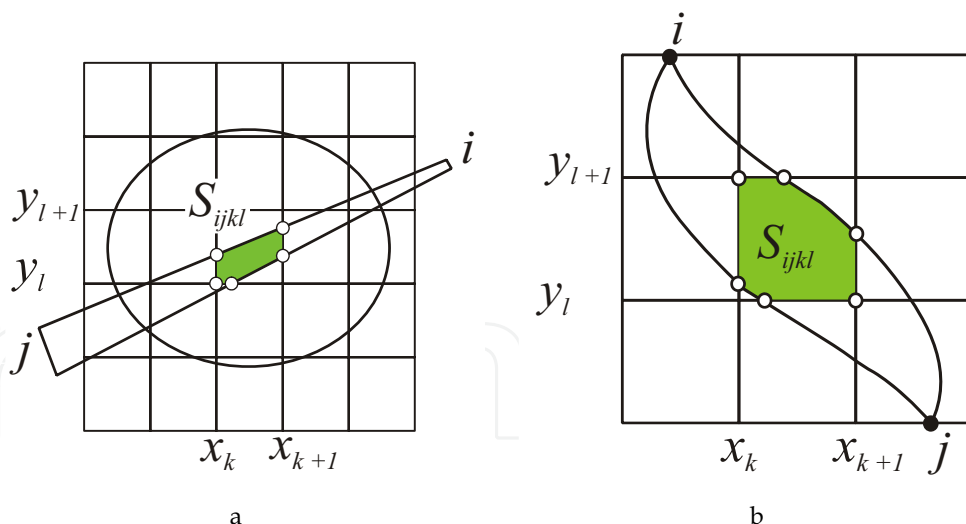


Figure 1. Calculation of weights: (a) X-ray tomography; (b) DOT

In this case, the matrix of coefficients of system (6) (hereafter, weight matrix) appears to be highly sparse because each trajectory intersects very few cells. This fact markedly worsens

convergence of algorithms used to solve system (6) that is strongly underdetermined due to incomplete data. To reduce the number of zero elements in the matrix, we modernized the method for calculation of W_{ijkl} having changed the infinite narrow trajectory by a strip of a finite width (Konovalov et al., 2006a; 2006b).

In X-ray tomography, the strip is a long trapeze (Figure 1(a)). Its bases are source aperture (the linear size of the focal spot) and receiver aperture (as a rule, the intrinsic resolution of the recording system). In this case, the weights can be calculated with the formula

$$W_{ijkl} = S_{ijkl} / \delta, \quad (7)$$

where S_{ijkl} is the area of intersection of the strip corresponding to i -source and j -receiver (hereafter, (i, j) -strip) with the (k, l) -cell, and δ is the linear size of the cell. It is obvious that the calculation of S_{ijkl} for trapezoidal strips must not cause difficulty.

The situation is more complicated in DOT. The configuration and size of the appropriate strip must be selected with account for the spatial distribution of the trajectories of photons migrating from the point $(\mathbf{r}_s, 0)$ to the point (\mathbf{r}_d, t) . According to the above statistical model, the most probable trajectories are distributed in a zone defined by the standard root-mean-square deviation (RMSD) from the PAT in accordance with the formula

$$\Delta(\tau) = \left\{ \int_V |\mathbf{r} - \mathbf{R}(\tau)|^2 P[\mathbf{r}, \tau | (\mathbf{r}_s, 0) \rightarrow (\mathbf{r}_d, t)] d^3r \right\}^{1/2}. \quad (8)$$

This zone is shaped as a banana (Lyubimov et al., 2002; Volkonskii, 1999) with vertices at the points of source and receiver localizations on the boundary of the scattering object. Therefore, for the (i, j) -strip we take a banana-shaped strip (Figure 1(b)) whose width is directly proportional to the RMSD: $\varepsilon(\tau) = \gamma \cdot \Delta(\tau)$. The problem is thus reduced to finding statistical characteristics (5) and (8) of photon trajectories. Note that the exact analytical calculation of $\mathbf{R}(\tau)$ and $\Delta(\tau)$ is difficult for even simple configurations such as a circle or a flat layer. The use of numerical techniques is undesirable because of the necessity to save computational time. Therefore, a number of simplifying assumptions should be done.

Lyubimov et al. (2002) and Volkonskii et al. (1999) propose to approximate the PAT by a three-segment broken line whose end segments are orthogonal to the boundary of the scattering object and the middle segment connects the end ones. This approach is effective if inhomogeneities are located inside the object, but causes distortions if inhomogeneities are near the boundaries where the PATs bend. In this chapter we configure banana-shaped strips in the geometry of a flat layer using a simplified analytical approach based on the analysis of PAT bending near a plane boundary. The approach uses the time-dependent radiation transport equation in the diffusion approximation. Konovalov et al. (2006b) showed that in the case where a instantaneous point source was in a homogeneous half-space (a half-plane in 2D) $y \geq 0$ at a point $(0, y_0)$ and a receiver was at a point $(x_0, 0)$ on the boundary $y = 0$, coordinates of the mass center of the distribution P , moving from the source point to the receiver point could be expressed as

$$\begin{cases} X(\tau) = x_0 \tau / t \\ Y(\tau) = y_0 \left\{ \left[1 + \frac{\tau}{t} \left(\frac{\alpha}{2} - 1 \right) \right] \operatorname{erf} \left(\frac{t - \tau}{\alpha \tau} \right)^{1/2} + \left[\frac{\alpha \tau (t - \tau)}{\pi t^2} \right]^{1/2} \exp \left(- \frac{t - \tau}{\alpha \tau} \right) \right\}, \end{cases} \quad (9)$$

where $\alpha = 4Kvt/y_0^2$, K is the diffusion coefficient of the media, $\operatorname{erf}(\xi)$ is the probability integral. If assume that PAT bending near the plane (straight line) of a source S is similar to bending near the plane (straight line) of a receiver D and there is no influence of the opposite boundary, analytical expressions (9) can be easily used to construct the PAT for the flat layer geometry (Figure 2). Indeed, the mass center passes the distance SO and the distance OD during the time $t/2$. If the mass center moved in the half-space $y \geq 0$ from a point S_0 to the point D through the point O , the time $t/2$ would correspond to the distance S_0O . Since component velocity along the X-axis is constant, the point S_0 lies on the perpendicular SS' to the media boundaries. The distance S_0S' can be found through the numerical solution of the equation $Y|_{\tau=t/2} = d/2$, where d is the width of the layer, for y_0 (see expressions (9)). After that the distance OD is calculated with (9) and the distance SO is obtained through its symmetric reflection about the point O .

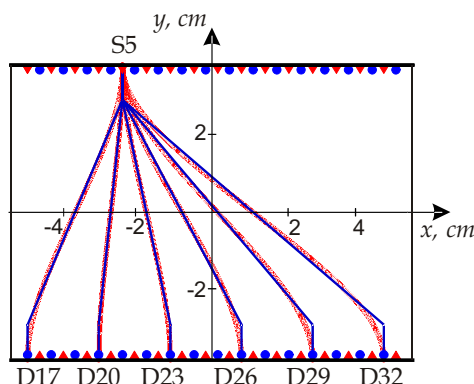
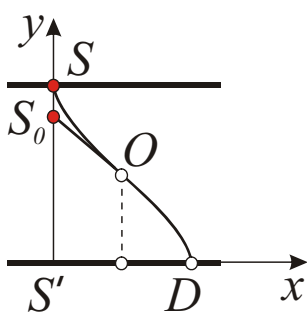


Figure 2. PAT construction for a flat layer

Figure 3. Geometry of data recording for a rectangular object

Figure 3 shows the geometry of data recording we chosen for simulations. Red triangles denote the positions of sources and blue circles do the positions of receivers. It also shows, as examples, six average trajectories reproduced with the above algorithm for $t = 3000$ ps and optical parameters $K = 0.066$ cm and $v = 0.0214$ cm/ps. Blue lines show piecewise-linear approximations of the PATs. Coordinates of the indicated sources and receivers (in centimeters) are as follows: S5 - (-2.52, 4), D17 - (-5, -4), D20 - (-3.06, -4), D23 - (-1.13, -4), D26 - (0.81, -4), D29 - (2.74, -4), D32 - (4.68, -4). In this chapter we study the probing regime in transmission, i.e. only relations between sources and receivers located on the opposite boundaries of the object are considered. The total number of average trajectories therefore

equals to 32×16 (32 sources and 16 receivers). In the reconstruction we will vary the number of sources to study how the spatial resolution depends on the degree of data incompleteness.

High accuracy of RMSD calculation is not crucial for the construction of banana-shaped strips. Therefore, in accordance with the inference of Volkonskii et al. (1999) that RMSD is actually independent of the form of the object, we can use the following simple formula for infinite space:

$$\Delta(\tau) \cong [2Kv(t - \tau)\tau / t]^{1/2}. \quad (10)$$

Boundaries of banana-shaped strips are defined as follows.

- (a) Define a set of discrete times $\{\tau_p\}$.
- (b) Construct perpendiculars to tangential lines at PAT points corresponding to times $\{\tau_p\}$ (Figure 4).
- (c) Lay off sections of the length $\varepsilon(\tau_p)$ in both directions along each perpendicular.
- (d) Construct lines connecting the points which we obtained for different $\{\tau_p\}$.

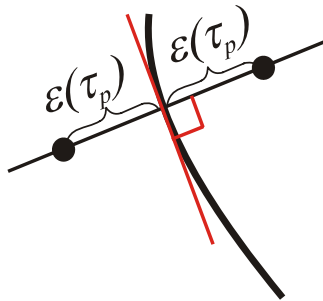


Figure 4. Definition of boundaries for banana-shaped strip

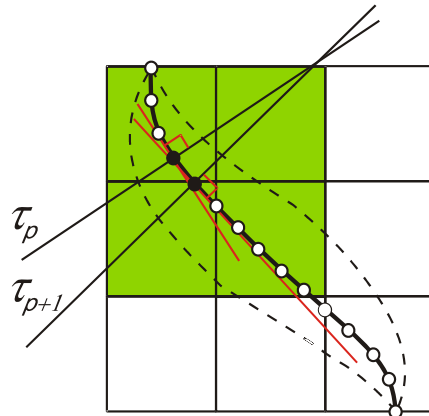


Figure 5. Definition of the discrete relative velocities of mass center of the distribution P

Boundaries of the strips are thus defined by piecewise-linear functions. To calculate the areas S_{ijkl} , we find the points where the strip boundaries intersect the sides of the cell. A polygon with vertices at the obtained points and cell nodes is treated as the intersection of the (i, j) -strip and the (k, l) -cell (Figure 1(b)). Weights are calculated with the formula

$$W_{ijkl} = S_{ijkl} / (v_{ijkl} \delta) \quad (11)$$

where v_{ijkl} is the discrete velocity of the mass center of the distribution P for the (i, j) -strip and the (k, l) -cell. Analytically, the velocities $v(\tau_p)$ are determined through

differentiation of expressions (9). The array of discrete values $\{v_{ijkl}\}$ is defined with the following algorithm.

- (a) Define a set of discrete times $\{\tau_p\}$.
- (b) Construct perpendiculars to tangential lines at points of L_{ij} corresponding to the times $\{\tau_p\}$ (Figure 5).
- (c) Assign a loop for p , in which the following sequence of steps is performed:
 - Find cells where the (i, j) -strip intercepts a strip created by two neighbor perpendiculars corresponding to the times τ_p and τ_{p+1} . In Figure 5, these cells are shown in green.
 - To all cells found, assign a value which equals the velocity averaged over two times: $[v(\tau_p) + v(\tau_{p+1})]/2$.
 - If some value v_{ijkl}^{old} has already been assigned to a cell, it is updated with the formula

$$v_{ijkl} = \frac{v_{ijkl}^{old} \cdot N + v_{ijkl}^{new}}{N + 1}, \quad (12)$$

where v_{ijkl}^{new} is the new value and N is the number of previous updates.

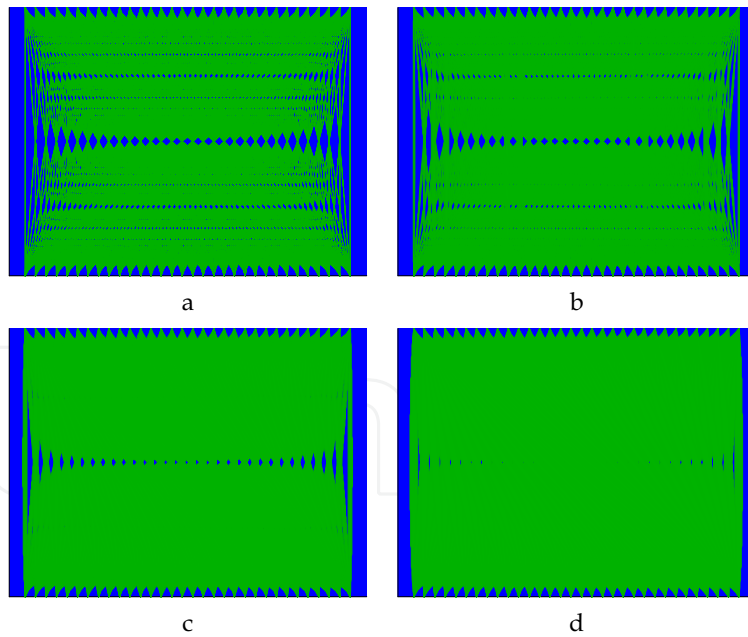


Figure 6. The area of the object filled with banana-shaped strips for different values of coefficient γ : (a) – 0; (b) – 0.05; (c) – 0.15; and (d) – 0.25

(d) All PATs are searched sequentially and, for each of them, the procedure is repeated beginning from step (b).

The proportionality coefficient $\gamma \in (0, 1)$ which defines the width of the banana-shaped strip is selected from a condition dictating that all strips must sufficiently fill the area of the object. Figure 6 shows the filling of the rectangular object presented in Figure 3 for ratio of sources and receivers (hereafter, measurement ratio) 32×16 and γ equal to 0, 0.05, 0.15, and 0.25. In Figure 6(a), (b), and (c), there are extended regions with no strips (shown in blue). This means that, if the grid is of high resolution, there are cells where corrections won't be introduced during the process of reconstruction. In Figure 6(d) these regions are very small in size which minimizes the probability that "dead" cells will appear. That is why we reconstruct the absorbing inhomogeneities embedded in the scattering object shown in Figure 3 using banana-shaped strips whose width is $\varepsilon(\tau) = 0.25\Delta(\tau)$.

It should be noted that the problem of area filling in FVCT is not as decisive as in DOT if even the strips are very narrow. Despite the small number of views, the number of strips corresponding to one view is rather large (> 100).

2.3 Algebraic reconstruction techniques and methods of their modification

When selecting an algorithm to invert system (6), we must remember that in case of very incomplete data, the system appears to be strongly underdetermined. That is why the problem of solution regularization is of great importance in the context of the need to approximate the solution correctly and hence, to obtain tomograms which are free of artifacts. It is well known that the minimum of artifacts corresponds to the minimum of information contained in images. Under these circumstances, it seems appropriate to do reconstruction with an approach based on entropy optimization (Levine & Tribus, 1978). In this chapter we study the multiplicative algebraic reconstruction technique (MART) which implements the entropy maximum method. The problem of solution regularization is formulated as follows. Find the array of values $\{f_{kl}\}$ which satisfies system (6) and the conditions

$$f_{kl} \geq 0, \quad \left(\sum_{k,l} f_{kl} \ln f_{kl} \right) \rightarrow \max. \quad (13)$$

For the purpose of comparison and to demonstrate advantages of the MART, we also consider a well-known additive algebraic reconstruction technique (AART) which does not optimize entropy.

Both MART and AART are based on an iterative procedure of correction of certain initial approximation $\{f_{kl}^{(0)}\}$. At each $(s+1)$ -iteration trajectories (strips) from one source only are considered. Thus, the correction is introduced into the elements of the approximation $\{f_{kl}^{(s)}\}$ which correspond to the cells intersected by the given strips. Upon a transition from one iteration to another, the sources are searched cyclically. Original formulas for the correction of the s -th approximation to the solution are written as follows (Herman, 1980)

$$\begin{aligned} \text{MART: } f_{kl}^{(s+1)} &= f_{kl}^{(s)} \cdot \left(g_{ij} / \sum_{k,l} W_{ijkl} f_{kl}^{(s)} \right)^{\lambda W_{ijkl} / \delta} \\ \text{AART: } f_{kl}^{(s+1)} &= f_{kl}^{(s)} + \lambda \frac{g_{ij} - \sum_{k,l} W_{ijkl} f_{kl}^{(s)}}{\|\mathbf{w}\|_F^2} W_{ijkl}, \end{aligned} \quad (14)$$

where $\lambda \in (0,1)$ is the parameter which controls the rate of iterative process convergence and $\|\cdot\|_F$ is the Frobenius norm.

Our experience of using the algebraic techniques in FVCT (Konovalov et al., 2006a) and DOT (Konovalov et al., 2006b; Lyubimov et al., 2002) suggests that a number of modifications to formulas (14) are needed to improve convergence in case of strongly incomplete data. So, expressions (14) does not allow for

(a) the non-uniform distributions of weight sums and solution correction numbers over the cells; and

(b) any a priori information on the spatial distribution of reproduced structures.

As a result, both algorithms including the MART with regularization (13) often converge to a wrong solution. Because of the incorrect redistribution of intensity, images exhibit distinct artifacts which are often present in the regions where the structures are actually absent.

To avoid these shortcomings, we here use the following formulas for modified algebraic techniques

Step 1

$$\begin{aligned} \text{MART: } f_{kl}^{(s+1)} &= w_{kl} \cdot f_{kl}^{(s)} \cdot \left(g_{ij} / \sum_{k,l} W_{ijkl} f_{kl}^{(s)} \right)^{\lambda W_{ijkl} / \tilde{W}_{kl}} \\ \text{AART: } f_{kl}^{(s+1)} &= w_{kl} \cdot \left(f_{kl}^{(s)} + \lambda \frac{g_{ij} - \sum_{k,l} W_{ijkl} f_{kl}^{(s)}}{\|\mathbf{w}\|_F^2} \cdot \frac{\delta W_{ijkl}}{\tilde{W}_{kl}} \right), \end{aligned} \quad (15)$$

where $\tilde{W}_{kl} = \sum_{i,j} W_{ijkl} / N_L$ is the reduced weight sum for the (k,l) -cell, N_L is the total number of strips used in reconstruction, and \mathbf{w} is the matrix of correction factors which allow for a priori information on the object function (see below).

Step 2

$$f_{kl}^{(s+1)} = \frac{1}{(2r+1)^2} \sum_{m=-r}^r \sum_{n=-r}^r f_{k+m,l+n}^{(s+1)} \text{norm}(\tilde{W}_{k+m,l+n}) \text{norm}(A_{k+m,l+n}), \quad (16)$$

where the integer r specifies the size $r \times r$ of the smoothing window, A_{kl} is the number of corrections to the solution element corresponding to the (k,l) -cell, and

$$\text{norm}(\xi_{kl}) = \left[\xi_{kl} - \min_{k,l}(\xi_{kl}) \right] / \left[\max_{k,l}(\xi_{kl}) - \min_{k,l}(\xi_{kl}) \right] \quad (17)$$

is the operator which normalizes the distributions $\{\tilde{W}_{kl}\}$ and $\{A_{kl}\}$.

Accounting for the distributions of reduced weight sums and correction numbers over the cells is most crucial for DOT where they are markedly non-uniform (Figure 7). Figure 8 shows an example of reconstruction of the scattering object with two circular absorbing inhomogeneities 0.8 cm in diameters (see Section 3.2). Here and after the red triangles represent the localizations of the sources used for reconstruction. The Figure demonstrates advantages of the modified MART. We have bad results without taking into account the distributions $\{\tilde{W}_{kl}\}$ and $\{A_{kl}\}$ (Figure 8 (b) and (c)).

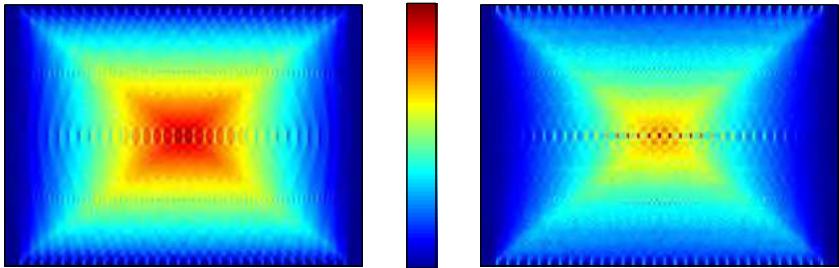


Figure 7. Distributions of reduced weight sums (a) and solution correction numbers (b) over 137×100 grid which cover the object shown in Figure 3

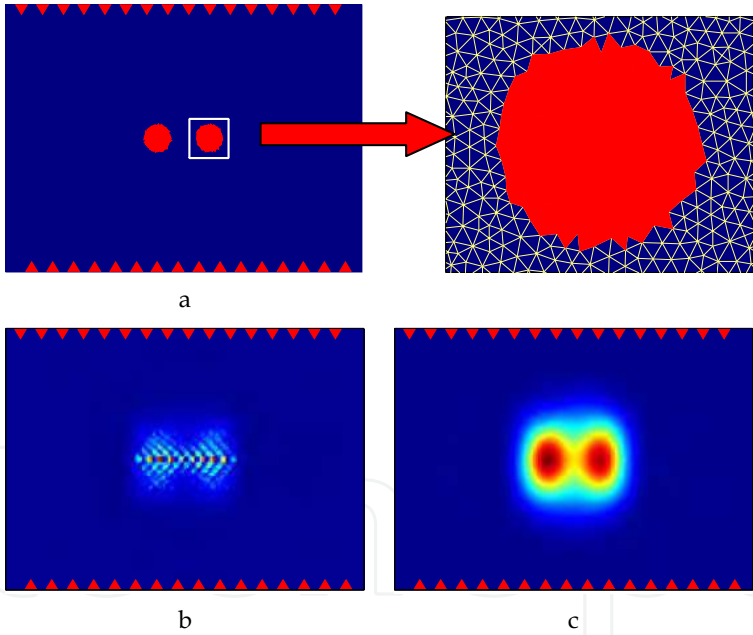


Figure 8. The 0.8-cm-in-diam absorbing inhomogeneities defined on a triangular mesh (a) and results of their reconstruction by the MART: without (b) and with (c) the distributions $\{\tilde{W}_{kl}\}$ and $\{A_{kl}\}$

To use a priori information on the presence of structure-free zones in the reconstruction region, we developed an algorithm illustrated by Figure 9 which shows the reconstruction

of the middle section of the iron sphere compressed by an explosion from radiographic data (see Section 3.1). The algorithm is described by the following sequence of steps:

(a) Reconstruct the image $\{f_{kl}^1\}$ from projections corresponding to the first source only (Figure 9 (a)).

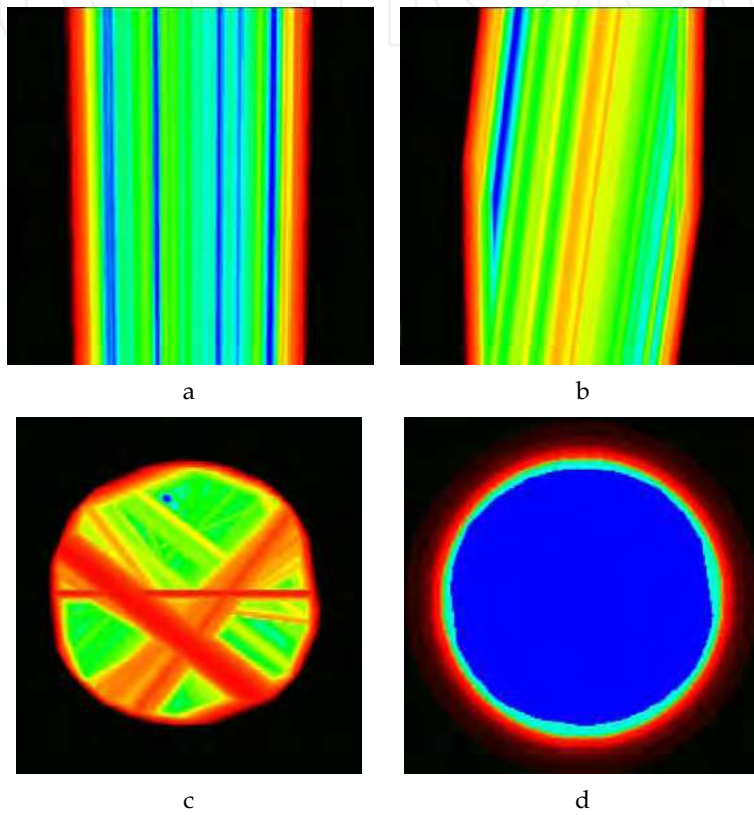


Figure 9. Generation of a useful part of the tomogram: (a) – the image $\{f_{kl}^1\}$; (b) – the image $\{\tilde{f}_{kl}^2\}$; (c) – the image $\{\tilde{f}_{kl}^{24}\}$; (d) – the set of multilevel regions

b) Reconstruct the image $\{f_{kl}^2\}$ from projections corresponding to the second source only and compare it with the result obtained at step (a). Following from the result of the comparison, form the image $\{\tilde{f}_{kl}^2\}$ such that $\tilde{f}_{kl}^2 = \min(f_{kl}^1, f_{kl}^2)$ for each (k, l) -cell (Figure 9(b)).

(c) Repeat step (b) for each following i -source forming the image $\{\tilde{f}_{kl}^i\}$ such that $\tilde{f}_{kl}^i = \min(\tilde{f}_{kl}^{i-1}, f_{kl}^i)$ (Figure 9(c)). Search all given sources.

(d) For the last image $\{\tilde{f}_{kl}^{last}\}$, define certain ascending sequence of relative thresholds $\{\varepsilon_m\}_1^M$, the largest of which does not exceed, for example, 0.1-0.2 and determine correction factors $\{w_{kl}\}$ using the following relations:

$$\begin{aligned} w_{kl} &= 0, & \text{if } \tilde{f}_{kl}^{last} < \varepsilon_1 \cdot \max\{\tilde{f}_{kl}^{last}\}, \\ w_{kl} &= \frac{\varepsilon_m}{\varepsilon_M} & \text{if } \varepsilon_m \cdot \max\{\tilde{f}_{kl}^{last}\} \leq \tilde{f}_{kl}^{last} < \varepsilon_{m+1} \cdot \max\{\tilde{f}_{kl}^{last}\} \\ w_{kl} &= 1, & \text{if } \tilde{f}_{kl}^{last} \geq \varepsilon_M \cdot \max\{\tilde{f}_{kl}^{last}\}. \end{aligned} \quad (18)$$

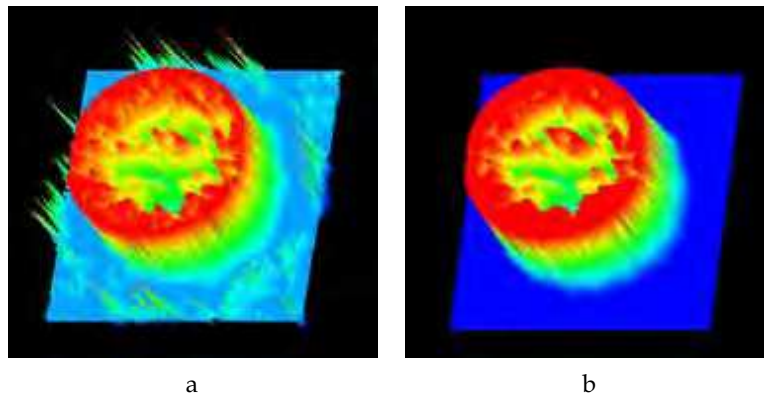


Figure 10. Reconstructions of the sphere section from 24 views by the MART without (a) and with (b) the correction factors $\{w_{kl}\}$

Such a definition of the set of multilevel regions with values that monotonically decrease from unity to zero (Figure 9(d)) allows artifacts to be avoided in the structure-free zones, i.e. where the object function must be zero or close to zero. The effect of accounting for $\{w_{kl}\}$ is demonstrated in Figure 10 which illustrates the reconstruction of the section of a sphere from 24 views by the MART. For visual demonstration, reconstructions are presented as surface plots.

It should be noted that in the case of the AART, it is also appropriate to use a priori information on whether the reconstructed object function is non-negative. For this end, all negative elements in the solution approximation are changed by zeros at each iteration. In the case of the MART, this is not needed because the algorithm works with a priori positive values.

3. Examples of reconstruction of test objects and quantitative analysis of tomograms

3.1 Reconstruction of strongly absorbing structures from few X-ray views

This section gives examples of 2D reconstruction of objects with strongly absorbing structures from experimental radiographic data. The objects include

(a) a foam plastic cylinder 6 cm in diameter with periodical spatial structures in the form of rows of coaxial thin steel rods whose diameters are 1.5, 2.5, 5 and 8 mm, and
(b) an iron sphere 4.8 cm in diameter with lots of internal damages from shock compression. X-ray projections are detected with a simple experimental setup (Figure 11 (a)). The radiation source is a pocket-size betatron with a small focal spot (about 1 mm) and a relatively small effective energy of the photon spectrum (about 2 MeV). The recording system combines a luminescent amplifying screen and an X-ray film. The object is placed between the source and the recording system so as to ensure that the film fully covers the object's shadow. To determine parameters of the characteristic curve of the recording system (photometric density versus exposure), we register the image of a step lead wedge with the object, as shown in Figure 11. Distances between the source and the object and between the source and the recording system are, respectively, 150 and 220 cm for the cylinder with periodic structures and 120 and 180 cm for the shocked sphere.

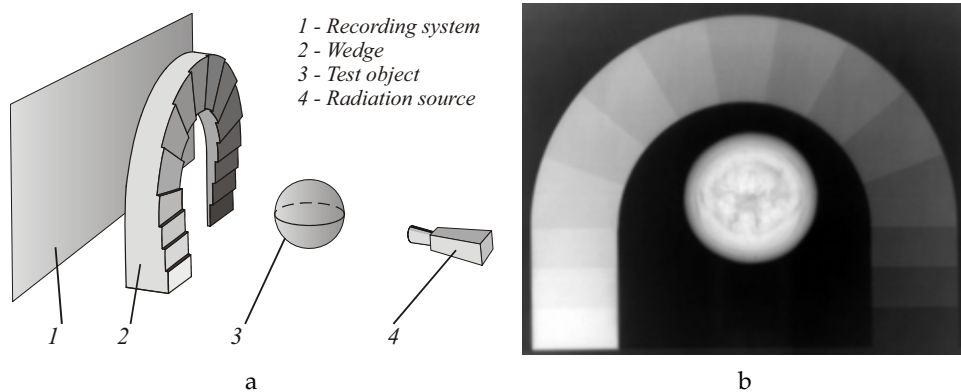


Figure 11. Experimental setup (a) and X-ray photograph of the shocked iron sphere (b)

To collect information, each film with the X-ray image is scanned using a laser scanner with a small focal spot. Digital data collected are converted from scanner counts into film exposures with a technique (Kozlovskii, 2006) developed and experimentally adjusted at Russian Federal Nuclear Center – Zababakhin Institute of Applied Physics. The technique is based on the approximation of the characteristic curve by the relation

$$I = I_0 + I_{\max} \exp(-a \cdot |b - \lg H|^c), \quad (19)$$

where I is the photometric density, H is the exposure, I_0 is a parameter which characterizes the density of film fogging, I_{\max} is a parameter which characterizes the maximum density the film permits, a and c are inclination and shape parameters, and b is a parameter which defines sensitivity of the recording system. The characteristic curve parameters I , I_{\max} , a , b and c are found through solving the problem of optimization for the objective function

$$\left[\frac{1}{Z} \sum_{i=1}^Z (I_i - I_i^{\text{meas}})^2 \right]^{1/2} \rightarrow \min, \quad (20)$$

where I_i is the photometric density calculated by expression (19) for i -step on the wedge, I_i^{meas} is the experimental density found with the image of the step wedge (Figure 11(b)) and Z is the number of steps on the wedge.

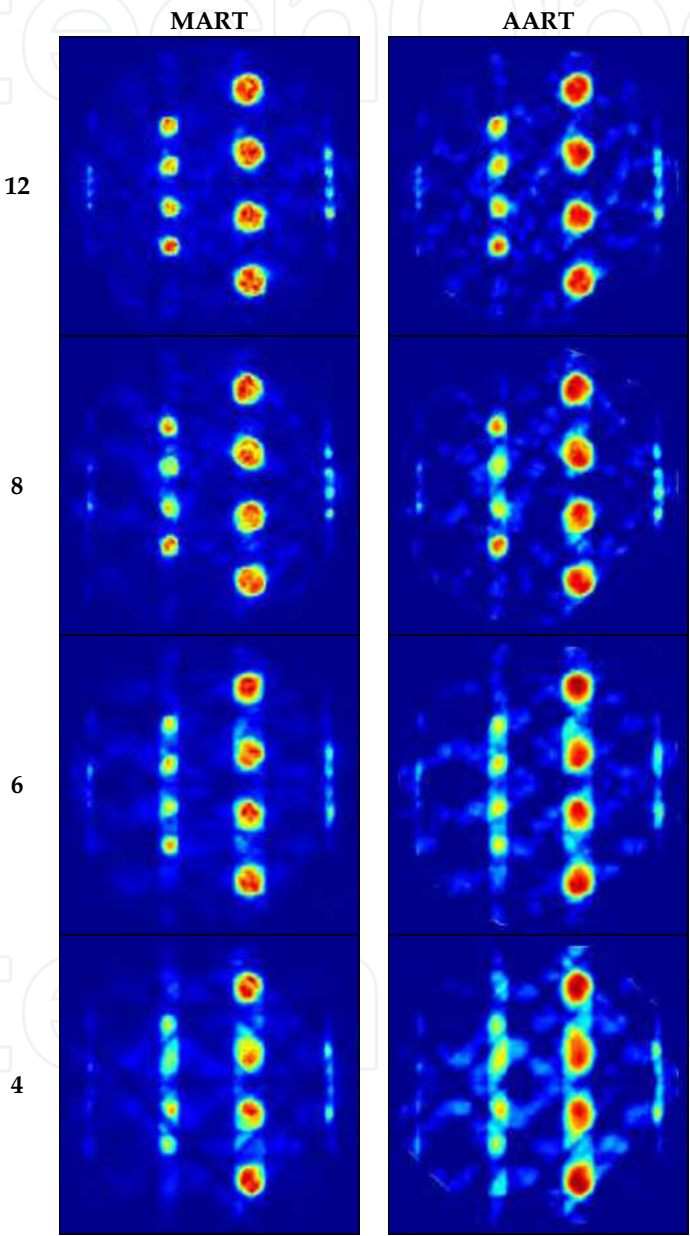


Figure 12. Tomograms of a cross section of the cylinder with periodic structures reconstructed from 12, 8, 6, and 4 views

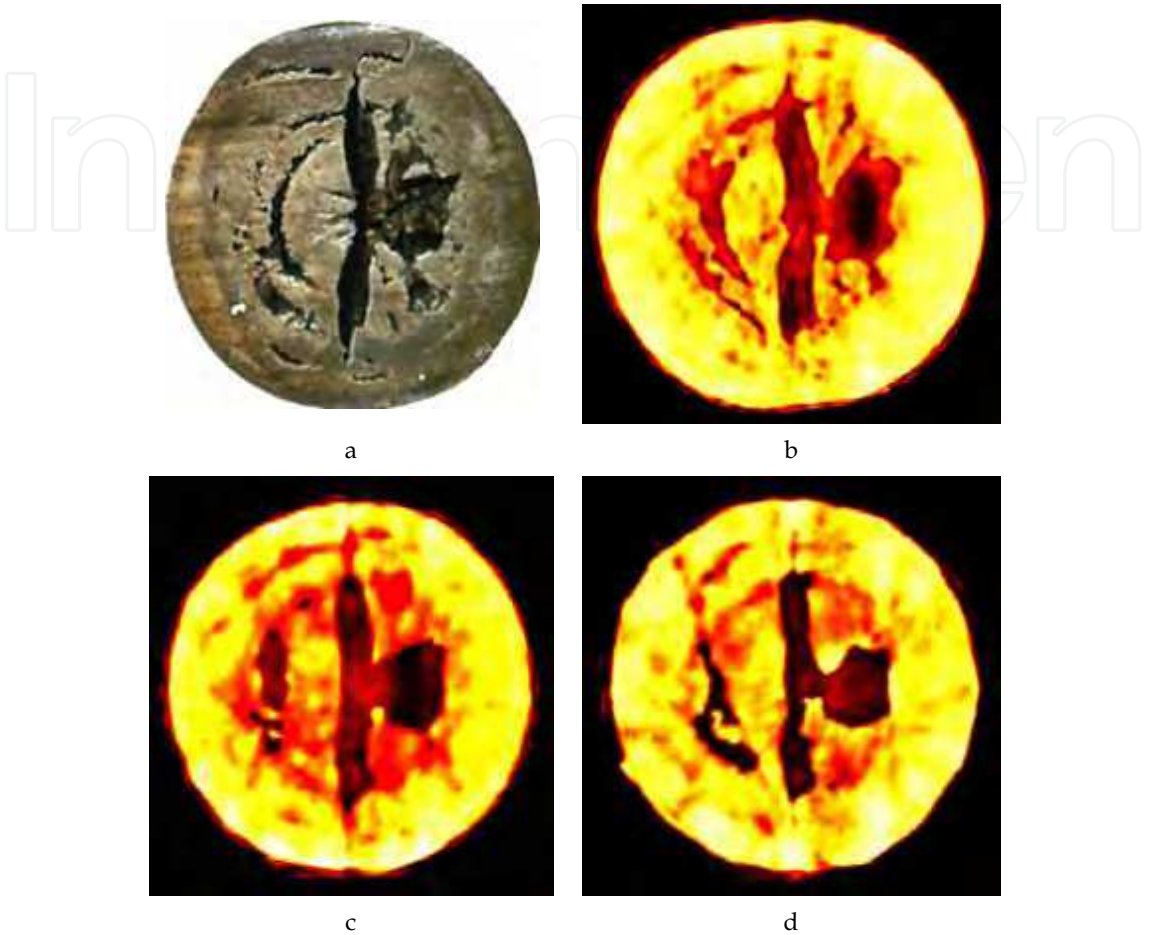


Figure 13. A photograph of the middle section of the sphere (a) and its reconstructions by the modified MART from 24 (b), 12 (c), and 8 (d) views

We assume that each X-ray in the conic beam is detected by a conventional receiver whose aperture is larger than the size of one cell of the digitized x-ray photograph. It is appropriate to take the aperture to be equal to the intrinsic resolution of the recording system. So, in order to calculate projections, we must average the exposures H over aperture areas. Projections are calculated as

$$g = -\log(H/H_0), \tag{21}$$

where H_0 is film exposure without the object (background).

Figure 12 shows the tomograms of a cross section of the cylinder with periodic structures reconstructed from the 1D arrays of projections by the modified MART and AART described in Section 2.3. On the left of the Figure there are the numbers of views used for the reconstruction. It is seen that the quality of reconstructions by the entropy optimizing

MART is a bit better than that of the images reconstructed by the AART. For the images shown in Figure 12, the visual resolution limit seems to be close to 1.5 mm because the row of 1.5-mm-diam rods is clearly seen in the upper images (MART, 12 and 8 views; AART, 12 views) and hardly distinguishable in the others. The quantitative analysis of spatial resolution is given in Section 3.3.

Figure 13 shows the tomograms of a middle section of the shocked sphere reconstructed by the modified MART in comparison with its photo taken after the sphere was cut with an electroerosion machine. It is seen from Figure 13 (a) and (b) that 24 views allow quite accurate reproduction of a fine fracture pattern (characterizing the reproduction of high-frequency structures) to be obtained. The images in Figure 13 (c) and (d) well reproduce the fracture pattern on whole, but small details are reproduced much worse compared with Figure 13(b).

Tomograms presented in Figure 13 qualitatively differ from those in Figure 12: the spatial structures in the sphere “drop” in reconstruction, i.e. the structures in the center are reproduced less intensively than the structures near its boundary. This is caused by the effect of beam hardening (Kak & Slanay, 1988) which distinctly manifests itself in the reconstruction of strongly absorbing objects. This proves that tomograms need post-processing.

3.2 Reconstruction of optical inhomogeneities embedded in strongly scattering media from model diffusion projections

To demonstrate efficiency of the modified algebraic algorithms for one-step reconstruction of diffuse optical tomograms, we conduct a numerical experiment where we simulate scattering objects with absorbing inhomogeneities and calculate diffusion projections. Four square objects $11 \times 8 \text{ cm}^2$ in size (Figure 3) are considered. Light velocity in the media and diffusion and absorption coefficients are 0.0214 cm/ps and 0.066 cm and 0.05 cm^{-1} , respectively. Each object has two circular inhomogeneities of identical diameters; they are near the center at a distance of one diameter from each other. Diameters of inhomogeneities in different objects are 1.2, 1.0, 0.8 and 0.6 cm. The inhomogeneity absorption coefficient is equal to 0.075 cm^{-1} . To simulate diffusion projections, we solve the time-dependent diffusion equation with the instantaneous point source

$$\frac{1}{v} \frac{\partial \varphi(\mathbf{r}, \tau)}{\partial \tau} - K \nabla^2 \varphi(\mathbf{r}, \tau) + [\mu_a + \delta\mu_a(\mathbf{r})] \varphi(\mathbf{r}, \tau) = \delta(\mathbf{r} - \mathbf{r}_s, \tau) \quad (22)$$

for the photon density $\varphi(\mathbf{r}, \tau)$ by the finite element method. The signal of the receiver is found with the formula

$$J(\mathbf{r}_d, t) = -K \frac{\partial \varphi(\mathbf{r}, \tau)}{\partial \eta} \bigg|_{\mathbf{r}=\mathbf{r}_d, \tau=t}, \quad (23)$$

where $\partial/\partial\eta$ is the derivative in the direction of the outer normal to the boundary of the object at the receiver point $\mathbf{r} = \mathbf{r}_d$. Accordingly, the diffusion projection $g(t)$ is found as logarithm of the ratio of the non-perturbed signal $J_0(t)$ calculated for the homogeneous medium to the signal $J(t)$ perturbed due to inhomogeneities.

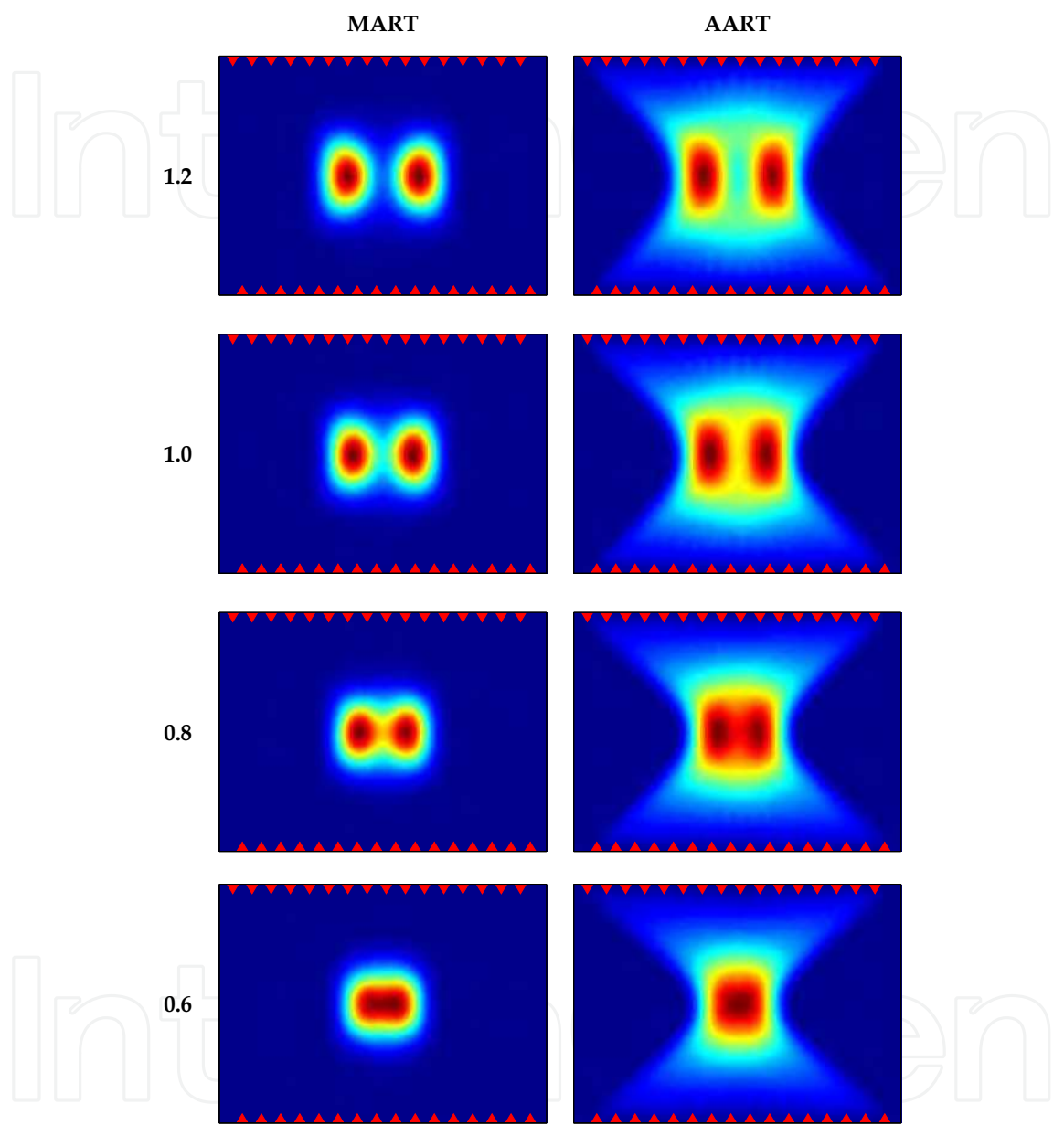


Figure 14. Reconstructions of scattering objects for measurement ratio 32×16

Figure 14 demonstrates the reconstructions of scattering objects by the modified MART and AART for measurement ratio 32×16 from diffusion projections calculated for the time-gating delay $t = 300$ ps. Diameters of inhomogeneities in cm are shown on the left of the Figure. It is seen that the AART that does not optimize entropy is a bit less accurate than the MART

in the reproduction of spatial structures. In all tomograms, inhomogeneities are deformed (elongated) because of averaging over the spatial distribution of photons. This makes it necessary to apply post-processing methods to neutralize such blur. To investigate how the degree of data incompleteness influences the quality of tomograms, we reconstruct scattering objects for measurement ratios 16×16 , 8×16 and 4×16 . As an example, Figure 15 shows a reconstructed object with inhomogeneities 0.8 cm in diameter. The number of sources is given on the left of the Figure. It is seen that in case of 4 sources (the lower row of images), the inhomogeneities are falsely shifted and not resolved relative each other in the case of the AART. The quantitative analysis of spatial resolution is discussed in Section 3.3.

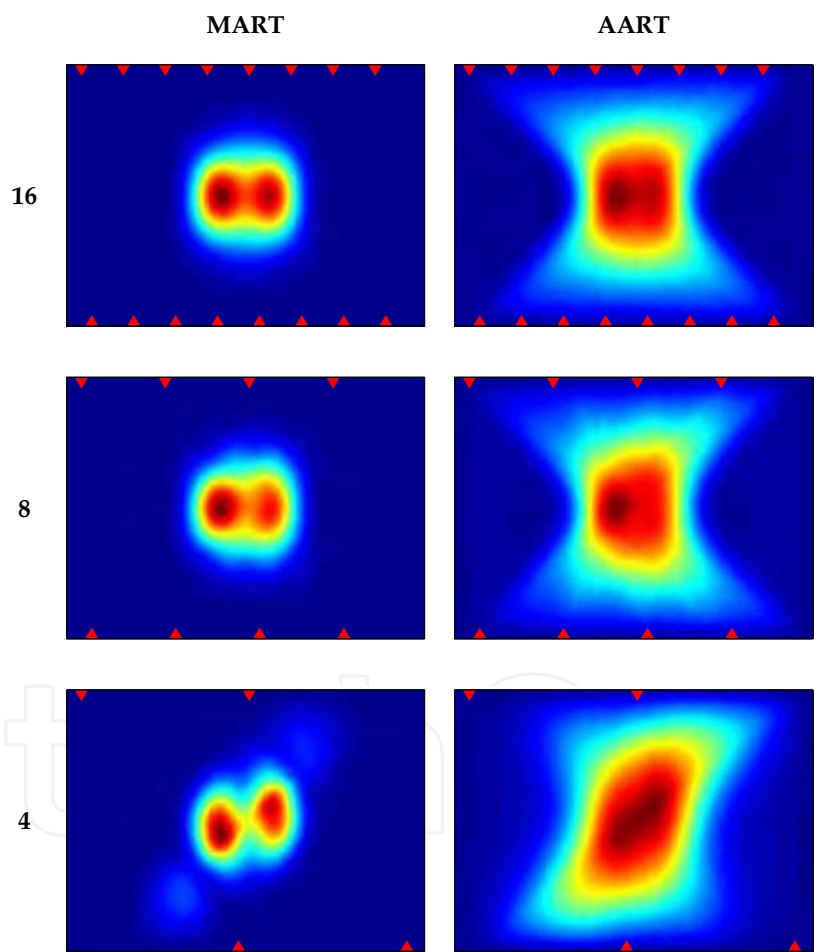


Figure 15. Reconstructions of the object with 0.8-cm-diam inhomogeneities for measurement ratios 16×16 , 8×16 , and 4×16

3.3 Quantitative analysis of tomogram resolution

In parallel beam projection tomography, the visualization system is usually described with a model of a linear filter invariant to spatial shift (Papoulis, 1968). The model allows the spatial resolution to be evaluated using a modulation transfer function (MTF) defined as the amplitude of system response to the harmonic signal. In the strict sense, the spatially invariant model is not applicable either in FVCT (because of fan beam geometry and strongly incomplete data), or in DOT (no regular straight photon trajectories). That is why, in this Section, we use the MTF only for the rough estimation of the resolution limit. On the contrary, in Section 4.1, blur of diffuse optical tomograms is neutralized with a spatially variant model which accounts for the dependence of spatial resolution on inhomogeneity localization.

To estimate the resolution from images of periodical spatial structures, we use the standard technique described, for example, by Konovalov et al. (2006a) and Lyubimov et al. (2002). From the profile of each reconstructed row of rods (Figure 12) or inhomogeneities (Figure 14 and Figure 15), we define the modulation transfer coefficient (MTC) as the average relative depth of the valley between peaks. The discrete spatial frequencies are assigned to diameters of the rods (inhomogeneities). A dependence of the MTC on spatial frequency is taken as an estimate to the MTF. Figure 16 (FVCT) and Figure 17 (DOT) illustrate the MTFs characterizing accuracy at which spatial structures are reconstructed from incomplete data by the modified MART and AART. It is seen that all curves from MART (red lines) run higher than those from AART (black lines), proving that the multiplicative algorithm that optimizes entropy is less restrictive in the reproduction of high-frequency spatial structures than the additive algorithm. So, for example, in reconstruction from 4 views (Figure 16(d)), 20% contrast (the conventional visual resolution limit (Papoulis, 1968)) corresponds to spatial frequencies 3.4 and 1.9 cycles/cm, if MART and AART are used. That is, if we are limited to 4 views, only spatial structures whose linear sizes are larger than 1.5 and 2.6 mm can be resolved in images reconstructed by the multiplicative and additive algebraic algorithms, respectively. Table 1 contains the estimates of the spatial resolution limit obtained in this manner from Figure 16 and Figure 17. Digits in brackets present similar estimates from the blue curves constructed for MART tomograms after space-varying restoration (see Section 4.1).

Tomography type	Number of views (sources)	Reconstruction technique	
		MART	AART
FVCT	12	1.0	1.5
	8	1.2	1.6
	6	1.4	2.5
	4	1.5	2.6
DOT	32	7.0 (6.0)	8.6
	16	8.1 (6.4)	10.0
	8	8.2 (6.8)	10.1
	4	9.0 (7.0)	12.6

Table 1. Estimated spatial resolution limit (in millimeters) for FVCT and DOT

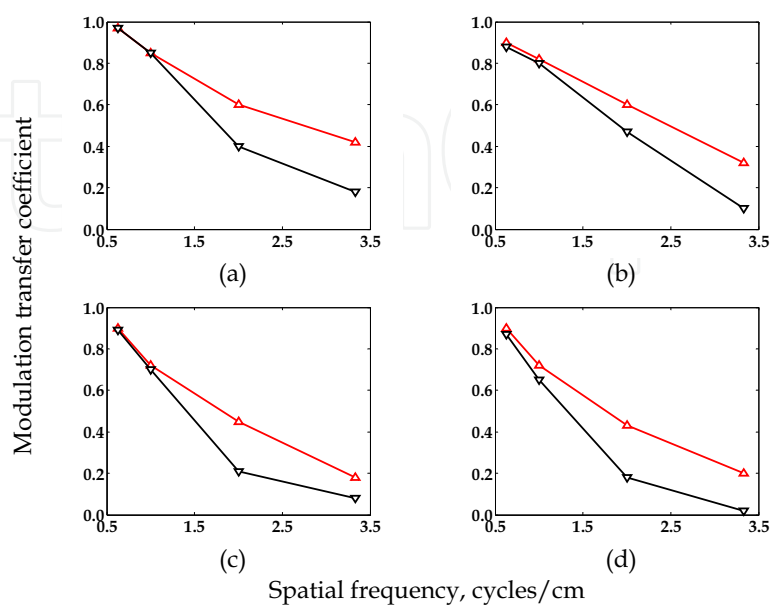


Figure 16. FVCT: MTFs for MART (red lines) and AART (black lines): (a) - 12; (b) - 8; (c) - 6; and (d) - 4 views

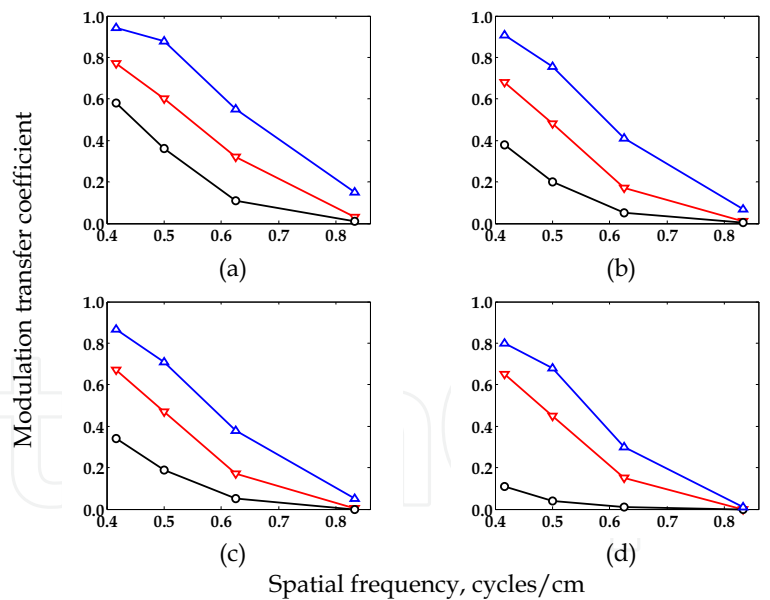


Figure 17. DOT: MTFs for MART (red lines), AART (black lines), and MART after restoration (blue lines): (a) - 32×16; (b) - 16×16; (c) - 8×16; and (d) - 4×16 sources and receivers

Analysis of data presented in the Table suggests that the use of the modified MART in FVCT helps get close to the resolution of medical X-ray tomography which uses the full set of

views. As for DOT, the resolution of the PAT method reached again with the modified MART is only slightly worse than the resolution of tomograms reconstructed by the multi-step reconstruction algorithms (Arridge, 1999) and there is still hope to improve it through post-processing.

4. Post-processing of tomograms

4.1 Space-varying restoration

As mentioned in Section 3.3, the strict description of the visualization system both in FVCT and DOT can only be made with a spatially variant blur model. In FVCT, spatial variance at a rough approximation can be neglected because the size of the object is small compared to source-object and object-receiver distances. In DOT, the strong dependence of structure reconstruction accuracy on structure localization directly follows from expressions (8) and (10) which characterize the theoretical limit of spatial resolution. The theoretical resolution tends to zero near boundaries. In the center, the resolution is worst and depends on the degree of data incompleteness (Table 1).

The traditional approach (Fish et al., 1996) to the restoration of images degraded by spatially variant blur is based on the assumption that blur is approximately spatially invariant in small regions of the image. Each such region is restored with its own spatially invariant point spread function (PSF) and results are then sewn together to obtain the full true image. This approach gives blocking artifacts at the region boundaries and they need to be removed by some means or other. In this chapter we restore diffusion tomograms using the blur model of Nagy et al. (2004). In accordance with the model, the image is divided into a number of regions where the PSF is approximately spatially invariant. However, instead of deblurring each region separately and then combining restoration results, the method interpolates individual invariant PSFs and restores the entire image. The discrete restoration problem for a tomogram with blur \mathbf{f} is described by a system of linear algebraic equations

$$\mathbf{f} = \mathbf{Q} \cdot \mathbf{z}, \quad (24)$$

where \mathbf{Q} is a large, ill-conditioned matrix describing the blurring operator and, \mathbf{z} is a discrete representation of the true image. Matrix \mathbf{Q} contains all non-zero elements of each of the spatially invariant PSF assigned to the individual regions of the tomogram. \mathbf{Q} also accounts for a priori information on the extrapolation of the restored image beyond its boundaries, i.e. boundary conditions. This is necessary to compensate for near-boundary artifacts caused by Gibbs effect. So, for example, in the case of reflexive boundary conditions that we use for restoration, \mathbf{Q} is the sum of the banded block Toeplitz matrix with banded Toeplitz blocks (Kamm & Nagy, 1998) and the banded block Hankel matrix with banded Hankel blocks (Ng et al., 1999).

Each spatially invariant PSF assigned to an individual region of the diffusion tomogram is simulated by performing the following sequence of steps.

(a) On a triangular mesh, we define a point inhomogeneity by three equal values in the nodes of a triangle located at the center of the region. The amplitude of the inhomogeneity is an order of magnitude larger than the amplitude $\delta\mu_a(\mathbf{r})$.

(b) Diffusion projections from the point inhomogeneity are simulated through the solution of equation (22) with the finite element method.

(c) A tomogram with PSF is reconstructed from obtained model projections by the modified algebraic techniques described above.

For the inversion of system (24), we selected the iterative residual norm steepest descent algorithm (Kaufman, 1993) that converges rather fast and has a semi-convergence with respect to the relative error $\|\mathbf{z}_s - \mathbf{z}\|/\|\mathbf{z}\|$, where \mathbf{z}_s is the approximation to \mathbf{z} on s -iteration. This is of great importance for getting the regularized solution. Here we omit details of the procedure used to restore diffuse optical tomograms reconstructed by the PAT method. They can be found in (Konovalov et al., 2007).

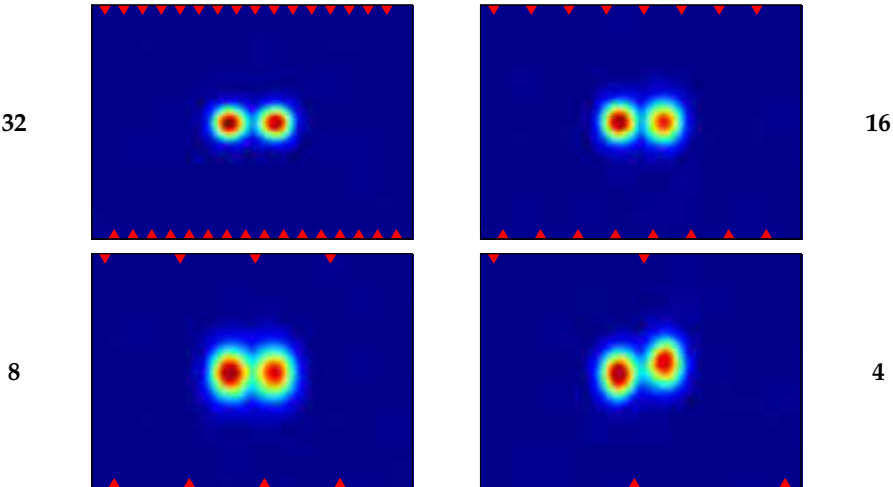


Figure 18. Results of space-varying restoration of MART-tomograms with 0.8-cm-diam inhomogeneities for measurement ratios 32×16, 16×16, 8×16, and 4×16

Figure 18 shows some results of space-varying restoration of diffusion tomograms reconstructed by the MART and presented in Figure 14 and Figure 15. The corresponding number of sources used for reconstruction and simulation of individual PSFs is given on the left and on the right of Figure 18. For restoration, a tomogram is divided into two conditionally spatially invariant regions, each of them containing its own absorbing inhomogeneity. To simulate the PSF, we defined a point inhomogeneity in a triangle located in the center of the inhomogeneity. It is seen from the Figure that we succeeded to not only improve resolution, but also neutralize deformations in the inhomogeneity shape. After restoration, the structures are reproduced much better even through the data are ultimately incomplete (see right image at the bottom of Figure 18). Blue curves in Figure 17 show MTFs constructed from the profiles of restored MART-tomograms. The corresponding estimates of spatial resolution provided in Table 1 in brackets demonstrate a significant gain in resolution (more than 16% for measurement ratio 32×16) due to space-varying restoration. It should be noted that the problem of restoration of spatially variant blur is also needed in FVCT. However, to get the effect here, the PSF must be defined for each image cell, as the resolution in FVCT is much better than that in DOT (see Table 1). It is extremely difficult to do because of enormous requirements for computing and time resources. Search for an acceptable solution which will help implement a spatially variant model in FVCT is the subject of our short-term interest.

4.2 Post-processing based on nonlinear color interpretation

The effect of gamma-quanta beam hardening (Figure 13) is caused by the polyenergetic spectrum of radiation source and dependence of the object function (extinction coefficient) on the photon energy. Existing methods for eliminating beam hardening artifacts fall into three categories: pre-processing of projection data (Brooks & Chiro, 1976; McDavid et al., 1977), iterative post-processing of reconstructed tomogram (Elbakri & Fessler, 2002; Yan et al., 2000) and dual-energy imaging (Alvarez & Macovski, 1976; Kak & Slaney, 1988; Konovalov et al., 1999; 2000). The pre-processing methods are low efficient when high-contrast structures are reconstructed. The most accurate iterative post-processing methods require, as a rule, extensive computation and turn out to be time-consuming. The dual-energy methods presuppose data recording for different spectra of radiation source, as well as additional calibration procedures to measure the effective photon energy (Konovalov et al., 1999; 2000).

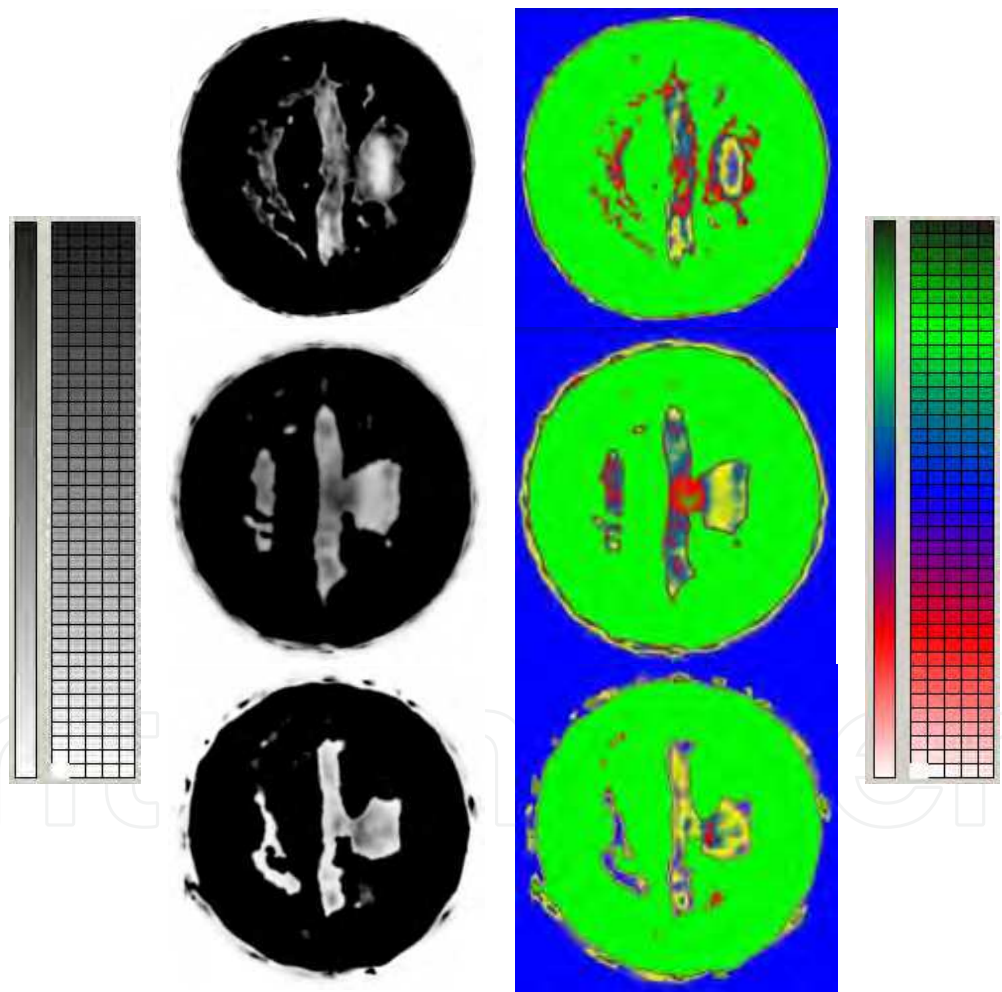


Figure 19. Results of application of linear (left) and nonlinear (right) palette to the images presented in Figure 13(b), (c), and (d)

For “flattening” the image intensity in order to compensate the beam hardening effect, we use simplified approach based on an application of the color interpretation methods. We consider the methods for creation of nonlinear color palettes and nonlinear statistical and analytical functions of correspondence between image intensity and color space. Detailed description of algorithms is given in (Mogilenskikh, 2000). This chapter is mainly focused on illustrative examples of their application.

The color palette is the ordered set of colors from the color space where each color corresponds to its own ordinal number. If the palette is nonlinear, the set of colors form a curvilinear trajectory in the color space. For image visualization with the use of the color palette we should form the law of correspondence between image intensities and colors in the cells (hereafter, correspondence function, CF). The argument value of such function is the image intensity, and the function value is the color or the color index in the palette. The linear CF is usually applied. Figure 19 shows the result of application of the linear black-and-white palette and the linear CF (left), as well as nonlinear palette including four basic colors (blue, yellow, red, and green) and the linear CF (right) to the tomograms given in Figure 13. It is seen that the fracture area is more obviously revealed in the second case.

However, the linear CF does not always allow data interpretation to be informative enough. To enhance the image informativity, we use the nonlinear statistical and analytical CF. The algorithm for creating the nonlinear statistical CF can be briefly described by the following sequence of steps.

- (a) Form the linear CF and put color $G(f_{kl})$ in conformity with image intensity f_{kl} in the (k, l) -cell.
- (b) Calculate the number of cells $N_G^{cells}(f_{kl})$ corresponding to each color of the palette and define the weights according to the formula

$$W_G(f_{kl}) = N_{col} \text{norm} \left[\frac{N_G^{cells}(f_{kl}) + 1}{N^{cells}} \right], \quad (25)$$

where N_{col} is a number of colors in the palette, N^{cells} is a full number of image cells, and $\text{norm}(\cdot)$ is normalization operator (17).

- (c) Calculate the statistical CF in the form of a spline. The following 1st degree spline is used in our case:

$$G^{stat}(f_{kl}) = [G(f_{kl}) - N_{col} \text{norm}(f_{kl})] \cdot [W_G(f_{kl}) - W_{G+1}(f_{kl})] + W_G(f_{kl}). \quad (26)$$

- (d) Form the nonlinear CF through addition of the statistical CF (step(c)) and the linear CF (step (a)).

Left column of images in Figure 20 demonstrates the example of application of such nonlinear CF to tomograms given in Figure 13. Thus, it is possible to automatically distinguish informative contours of fractures and simultaneously preserve intensity shades inside the image.

The essence of analytical CF is in applying the nonlinear color coordinate scales to attain the correspondence between the color and the intensity in the cells. Elementary functions and their algebraic combinations are used for that. Right column of images in Figure 20 shows the result of application of exponential CF $G(f) = \exp(60f)$ to images given in Figure 19

on the left. The type of the function is selected on the basis of the a priori information on the homogeneity of high-density structures of the object, which helps to present the internal facture pattern in the palette of two colors: black and white. This allows the informative regions of cracks and their boundaries to be strongly distinguished.

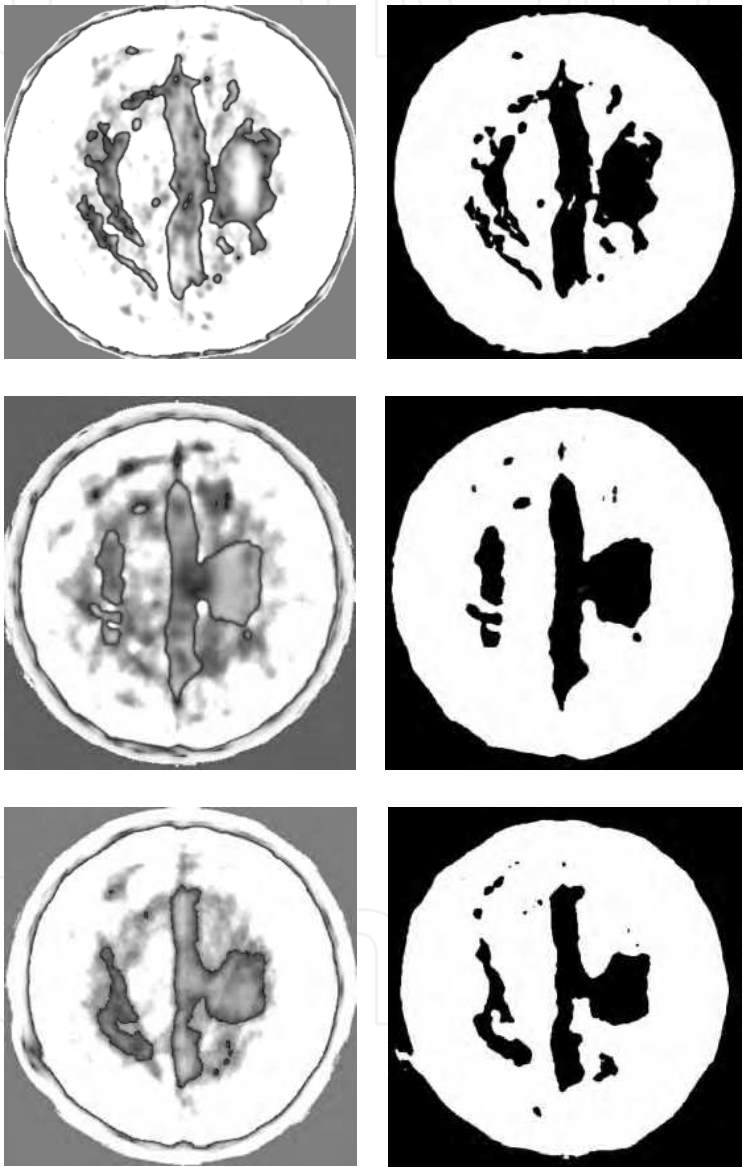


Figure 20. Results of application of statistical (left) and analytical (right) CF to the images presented in Figure 13 and 19 (on the left), respectively

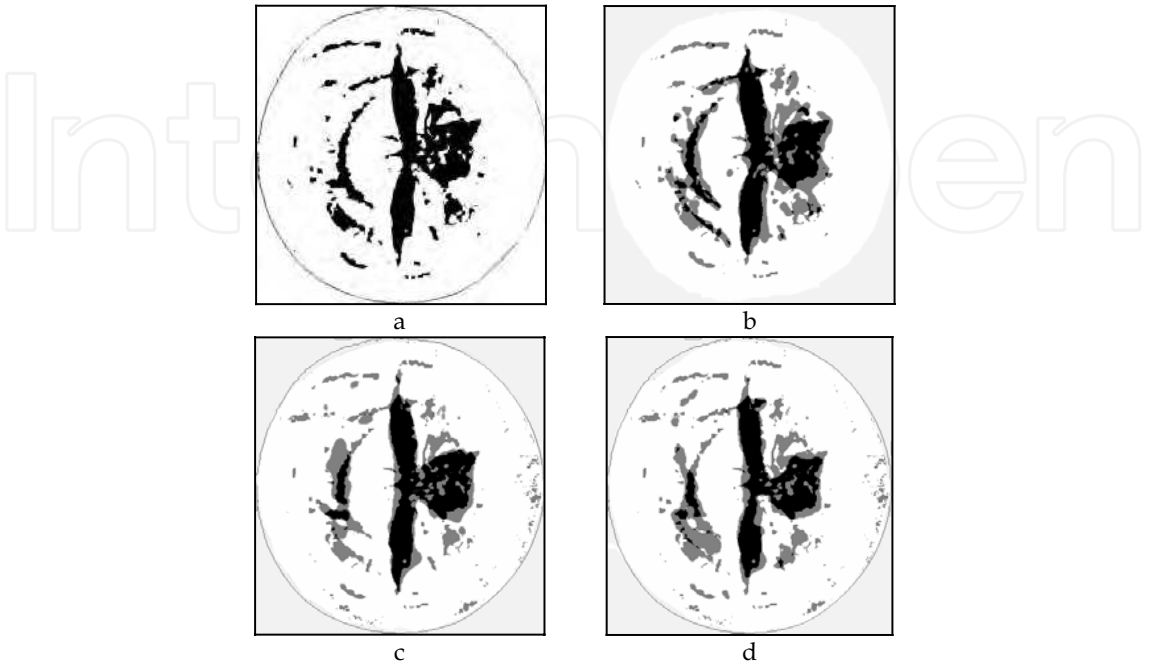


Figure 21. The processed photograph of sphere section (a) and the results of binary operations with processed tomograms reconstructed from 24 (b), 12 (c), and 8 (d) views

To estimate the accuracy of fracture pattern reproduction, we compare the results of tomogram post-processing with the etalon image obtained through processing of the photo presented in Figure 13(a). For comparison, a variety of methods based on binary operations and visualization algorithms (Mogilenskikh & Pavlov, 2002; Mogilenskikh, 2003) can be used. In our case, processing of the photo includes the construction of the same-level isolines, clearing of half-tones between the isolines, and filling of the isolines-bounded areas by black (Figure 21(a)). The processed photo is superimposed onto the processed tomograms given in Figure 20 on the right. As a result of binary operations, one obtains three-tone images presented in Figure 21(b), (c), and (d), where gray color characterizes the difference, and black and white – coincidence. The relations between gray areas and black area of the etalon image are equal to 0.03, 0.19, and 0.28, respectively. These quantitative estimates and visual analysis of Figure 21 show that the accuracy of reproduction of the fine fracture pattern seems to be unsatisfactory for reconstructions by 12 (Figure 21(c)) and 8 views (Figure 21(d)). This conclusion is in agreement with the results of Table 1, which show that the spatial resolution limit is worse than 1.0 mm when the number of views does not exceed 12.

The methods for creating the nonlinear CF are also efficient in the case of the diffusion tomograms post-processing. The space-varying restoration of tomograms obviously improves but still reproduces incomplete profile of inhomogeneities. And as it follows from Figure 22, nonlinear-CF-based processing of restored tomogram of the scattering object with 0.8-cm-diam inhomogeneities makes it possible to approach a “flat region” of the true profile.

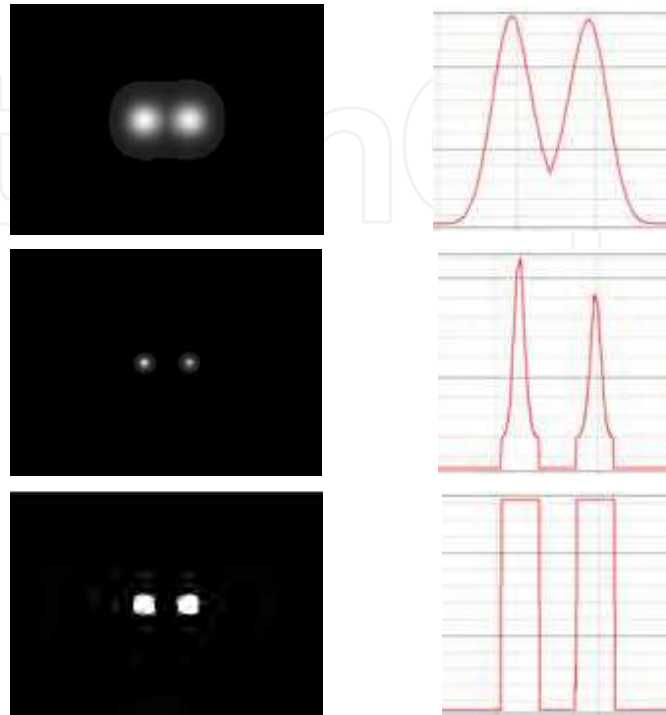


Figure 22. MART-tomogram with 0.8-cm-diam inhomogeneities and its profile after restoration (top), application of exponential CF $G(f) = \exp(14f)$ (center), and application of nonlinear statistical CF

5. Conclusion

In this chapter we consider two examples of algebraic reconstruction in incomplete data computed tomography: few-view X-ray computed tomography and one-step diffuse optical tomography. Multiplicative algebraic reconstruction technique optimizing the entropy allows the better quality of tomograms to be obtained. It is shown that, to enhance the convergence of iterative reconstruction procedure and to minimize the artifact level on tomograms, the conventional formulas of solution correction should be modified. The presented results of reconstruction demonstrate the efficiency of the following our modifications:

- (a) To calculate the weight matrix, we use not the lines but the narrow strips which provide the sufficient filling of the reconstruction area.
 - (b) We take into account the non-uniformity of the distributions of the weight sums and the solution corrections numbers over the image elements.
 - (c) We calculate the correction factors which account for a priori information on whether the solution is non-negative and on the presence of structure-free zones in the reconstruction area.
- For increasing the accuracy of spatial structures reproduction under conditions of the strong incompleteness of data, it is advisable to post-process the reconstructed tomograms with the

use of a priori information about the object. We demonstrate the efficiency of the methods of space-varying restoration and post-processing with nonlinear palette and nonlinear function of correspondence between the palette color and image intensity in the cells. As a result, we obtain the reproduction quality close to that of medical tomograms in the case of few-view tomography and close to quality of diffusion tomograms reconstructed by well-designed multi-step algorithms in the case of diffuse optical tomography.

In conclusion it should be noted that, for calculation, we use a rather slow soft-ware medium like MATLAB and a Windows XP Intel PC with 1.7-GHz Pentium 4 processor and 256-MB RAM. Computational time of the reconstruction-restoration procedure for diffuse optical tomograms is 1.5...2.5 minutes. These digits are better than those for multi-step reconstruction, but they do not satisfy the requirements of real-time medical explorations. In the future, it is interesting to optimize the duration of the diffuse optical image production. The implementation of a spatially variant blur model in few-view computed tomography is also the subject of our short-term interest.

6. Acknowledgements

The authors would like to thank S. P. Antipinskii, E. A. Averyaskin, S. A. Brichikov, V. V. Fedorov, D. M. Gorbachev, S. V. Kolchugin, E. V. Kovalev, E. A. Kozlov, V. M. Kryukov, I. V. Matveenkov, A. V. Mikhaylov, L. A. Panchenko, V. N. Povyshev, G. N. Rykovanov, V. V. Smirnov, T. V. Stavrietskaya, V. I. Stavrietskii, T. A. Strizhenok, A. B. Zalozhenkov, and M. N. Zakharov for collaboration in X-ray radiography and few-view computed tomography. The authors also thank A. G. Kalintsev, O. V. Kravtsenyuk, V. V. Lyubimov, A. G. Murzin, and L. N. Soms whose contribution to theory of the photon average trajectories method cannot be overemphasized.

7. References

- Alvarez, R. E. & Macovski, A. (1976). Energy-selective reconstruction in X-ray computerized tomography. *Physics in Medicine & Biology*, Vol. 21, No. 5, September 1976, pp. 733-744.
- Arridge, S. R. (1999). Optical tomography in medical imaging. *Inverse Problems*, Vol. 15, No. 2, April 1999, pp. R41-R93.
- Brooks, R. A. & Di Chiro, G. (1976). Beam hardening in X-ray reconstructive tomography. *Physics in Medicine & Biology*, Vol. 21, No. 3, May 1976, pp. 390-398.
- Devaney, A. J. (1983). A computer simulation study of diffraction tomography. *IEEE Transaction on Biomedical Engineering*, Vol. 30, No. 7, July 1983, pp. 377-386.
- Elbakri, I. A. & Fessler, J. A. (2002). Statistical image reconstruction for polyenergetic X-ray computed tomography. *IEEE Transactions on Medical Imaging*, Vol. 21, No. 2, February 2002, pp. 89-99.
- Fish, D. A.; Grochmalicki, J. E. & Pike, R. (1996). Scanning singular-value-decomposition method for restoration of images with space-variant blur. *Journal of the Optical Society of America A: Optics, Image Science & Vision*, Vol. 13, No. 3, March 1996, pp. 464-469.
- Hanson, K. M.; Bradbury, J. N.; Cannon, T. M.; Hutson, R. L.; Laubacher, D. B.; Macek, R. J.; Paciotti, M. A. & Taylor, C. A. (1981). Computed tomography using proton energy loss. *Physics in Medicine & Biology*, Vol. 26, No. 6, November 1981, pp. 965-983.

- Hanson, K. M.; Bradbury, J. N.; Koeppe, R. A.; Macek, R. J.; Machen, D. R.; Morgado, R.; Paciotti, M. A.; Sandford, S. A. & Steward, V. W. (1982). Proton computed tomography of human specimens. *Physics in Medicine & Biology*, Vol. 27, No. 1, January 1982, pp. 25-36.
- Hawrysz, D. J. & Sevic-Muraca, E. M. (2000). Developments toward diagnostic breast cancer imaging using near-infrared optical measurements and fluorescent contrast agents. *Neoplasia*, Vol. 2, No. 5, September 2000, pp. 388-417.
- Herman, G. T. (1980). *Image Reconstruction from Projections: The Fundamentals of Computerized Tomography*, Academic, New York.
- Kak, A. C. & Slaney, M. (1988). *Principles of Computerized Tomographic Imaging*, IEEE Press, New York.
- Kamm, J. & Nagy, J. G. (1998). Kronecker product and SVD approximation in image restoration. *Linear Algebra & Its Applications*, Vol. 284, No. 1-3, November 1998, pp. 177-192.
- Kaufman, L. (1993). Maximum likelihood, least squares, and penalized least squares for PET. *IEEE Transactions on Medical Imaging*, Vol. 12, No. 2, February 1993, pp. 200-214.
- Konovalov, A. B.; Volegov, P. L.; Kochegarova, L. P. & Dmitrakov, Yu. L. (1999). Determination of component concentrations in mixtures of organic liquids using a computer tomograph. *Journal of Analytical Chemistry*, Vol. 54, No. 4, April 1999, pp. 315-319.
- Konovalov, A. B.; Volegov, P. L. & Dmitrakov, Yu. L. (2000). A simple method for CT-scanner calibration against effective photon energy. *Instruments & Experimental Techniques*, Vol. 43, No. 3, May 2000, pp. 398-402.
- Konovalov, A. B.; Lyubimov, V. V.; Kutuzov, I. I.; Kravtzenyuk, O. V.; Murzin, A. G.; Mordvinov, G. B.; Soms, L. N. & Yavorskaya, L. M. (2003). Application of the transform algorithms to high-resolution image reconstruction in optical diffusion tomography of strongly scattering media. *Journal of Electronic Imaging*, Vol. 12, No. 4, October 2003, pp. 602-612.
- Konovalov, A. B.; Kiselev, A. N. & Vlasov, V. V. (2006a). Spatial resolution of few-view computed tomography using algebraic reconstruction techniques. *Pattern Recognition & Image Analysis*, Vol. 16, No. 2, April 2006, pp. 249-255.
- Konovalov, A. B.; Vlasov, V. V.; Kalintsev, A. G.; Kravtzenyuk, O. V. & Lyubimov, V. V. (2006b). Time-domain diffuse optical tomography using analytic statistical characteristics of photon trajectories. *Quantum Electronics*, Vol. 36, No. 11, November 2006, pp. 1048-1055.
- Konovalov, A. B.; Vlasov, V. V.; Kravtzenyuk, O. V. & Lyubimov, V. V. (2007). Space-varying iterative restoration of diffuse optical tomograms reconstructed by the photon average trajectories method. *EURASIP Journal on Advances in Signal Processing*, Vol. 2007, No. 1, January 2007, ID 34747.
- Kozlovskii, V. N. (2006). *Information in Pulsed Radiography*, RFNC-VNIITF publisher, Snezhinsk (in Russian).
- Levine, R. D. & Tribus, M. (1978). *The Maximum Entropy Formalism*, MIT, Cambridge, MA.

- Lyubimov, V. V.; Kalintsev, A. G.; Konovalov, A. B.; Lyamtsev, O. V.; Kravtsenyuk, O.V.; Murzin, A. G.; Golubkina, O. V.; Mordvinov, G. B.; Soms, L. N. & Yavorskaya, L. M. (2002). Application of photon average trajectories method to real-time reconstruction of tissue inhomogeneities in diffuse optical tomography of strongly scattering media. *Physics in Medicine & Biology*, Vol. 47, No. 12, June 2002, pp. 2109-2128.
- Lyubimov, V. V.; Kravtsenyuk, O. V.; Kalintsev, A. G.; Murzin, A. G.; Soms, L. N.; Konovalov, A. B.; Kutuzov, I. I.; Golubkina O. V. & Yavorskaya, L. M. . (2003). The possibility of increasing the spatial resolution in diffusion optical tomography. *Journal of Optical Technology*, Vol. 70, No. 10, October 2003, pp. 715-720.
- McDavid, W. D.; Waggener, R. G.; Payne, W. H. & Dennis, M. J. (1977). Correction of spectral artifacts in cross-sectional reconstruction from X-rays. *Medical Physics*, Vol. 4, No. 1, January 1977, pp. 54-57.
- Mogilenskikh, D. V. (2000). Nonlinear color interpretation of physical processes, *Proceedings of International Conference on Computer Graphics "Graphicon'2000"*, pp. 201-211, Moscow, August-September 2000, Moscow State University publisher, Moscow.
- Mogilenskikh, D. V. & Pavlov, I. V. (2002). Color interpolation algorithms in visualizing results of numerical simulations, In: *Visualization and Imaging in Transport Phenomena*, Sideman, S. & Landesberg, A. (Eds.), *Annals of the New York Academy of Sciences*, Vol. 972, Part. 1, pp. 43-52, New York Academy of Sciences, New York.
- Mogilenskikh, D. V. (2003). "CONTOUR" algorithm for finding and visualizing flat sections of 3D-objects, In: *Computer Science and Its Applications*, Kumar, V. et al. (Eds.), *Lecture Notes in Computer Science*, Vol. 2669, pp. 407-417, Springer-Verlag, Berlin/Heidelberg.
- Nagy, J. G.; Palmer, K. & Perrone, L. (2004). Iterative methods for image deblurring: a Matlab object oriented approach. *Numerical Algorithms*, Vol. 36, No. 1, May 2004, pp. 73-93.
- Ng, M. K.; Chan, R. H. & Tang, W.-C. (1999). A fast algorithm for deblurring models with Neumann boundary conditions. *SIAM Journal on Scientific Computing*, Vol. 21, No. 3, November-December 1999, pp. 851-866.
- Palamodov, V. P. (1990). Some singular problems in tomography, In: *Mathematical Problems of Tomography*, Gel'fand, I. M. et al. (Eds.), *Transactions of Mathematical Monographs*, Vol. 81, pp. 123-139, American Mathematical Society, Providence, R. I.
- Papoulis, A. (1968). *Systems and Transforms with Applications in Optics*, McGraw-Hill, New York.
- Pickalov, V. V. & Melnikova, T. S. (1995). *Plasma Tomography*, Nauka, Novosibirsk (in Russian).
- Subbarao, P. M. V.; Munshi, P. & Muralidhar, K. (1997). Performance of iterative tomographic algorithms applied to non-destructive evaluation with limited data. *Nondestructive Testing & Evaluation International*, Vol. 30, No. 6, December 1997, pp. 359-370.
- Volkonskii, V. B.; Kravtsenyuk, O. V.; Lyubimov, V. V.; Mironov, E. P. & Murzin, A. G. (1999). The use of the statistical characteristics of the photons trajectories for the tomographic studies of the optical macroheterogeneities in strongly scattering objects. *Optics & Spectroscopy*, Vol. 86, No. 2, February 1999, pp. 253-260.
- Yan, C. H.; Whalen, R. T.; Beaupre, G. S.; Yen, S. Y. & Napel, S. (2000). Reconstruction algorithm for polychromatic CT imaging: application to beam hardening correction. *IEEE Transactions on Medical Imaging*, Vol. 19, No. 1, January 2000, pp. 1-11.
- Yodh, A. & Chance, B. (1995). Spectroscopy and imaging with diffusing light. *Physics Today*, Vol. 48, No. 3, March 1995, pp. 34-40.



Vision Systems: Applications

Edited by Goro Obinata and Ashish Dutta

ISBN 978-3-902613-01-1

Hard cover, 608 pages

Publisher I-Tech Education and Publishing

Published online 01, June, 2007

Published in print edition June, 2007

Computer Vision is the most important key in developing autonomous navigation systems for interaction with the environment. It also leads us to marvel at the functioning of our own vision system. In this book we have collected the latest applications of vision research from around the world. It contains both the conventional research areas like mobile robot navigation and map building, and more recent applications such as, micro vision, etc. The first seven chapters contain the newer applications of vision like micro vision, grasping using vision, behavior based perception, inspection of railways and humanitarian demining. The later chapters deal with applications of vision in mobile robot navigation, camera calibration, object detection in vision search, map building, etc.

How to reference

In order to correctly reference this scholarly work, feel free to copy and paste the following:

Alexander B. Konovalov, Dmitry V. Mogilenskikh, Vitaly V. Vlasov and Andrey N. Kiselev (2007). Algebraic Reconstruction and Post-Processing in Incomplete Data Computed Tomography: from X-rays to Laser Beams, Vision Systems: Applications, Goro Obinata and Ashish Dutta (Ed.), ISBN: 978-3-902613-01-1, InTech, Available from:

http://www.intechopen.com/books/vision_systems_applications/algebraic_reconstruction_and_post-processing_in_incomplete_data_computed_tomography__from_x-rays_to_

INTECH
open science | open minds

InTech Europe

University Campus STeP Ri
Slavka Krautzeka 83/A
51000 Rijeka, Croatia
Phone: +385 (51) 770 447
Fax: +385 (51) 686 166
www.intechopen.com

InTech China

Unit 405, Office Block, Hotel Equatorial Shanghai
No.65, Yan An Road (West), Shanghai, 200040, China
中国上海市延安西路65号上海国际贵都大饭店办公楼405单元
Phone: +86-21-62489820
Fax: +86-21-62489821

© 2007 The Author(s). Licensee IntechOpen. This chapter is distributed under the terms of the [Creative Commons Attribution-NonCommercial-ShareAlike-3.0 License](https://creativecommons.org/licenses/by-nc-sa/3.0/), which permits use, distribution and reproduction for non-commercial purposes, provided the original is properly cited and derivative works building on this content are distributed under the same license.

IntechOpen

IntechOpen